Aerospace Science and Technology 79 (2018) 297–309

Contents lists available at ScienceDirect

Aerospace Science and Technology

www.elsevier.com/locate/aescte

A study on adaptive vibration control and energy conversion of highly flexible multifunctional wings

Natsuki Tsushima, Weihua Su *

Department of Aerospace Engineering and Mechanics, University of Alabama, Box 870280, Tuscaloosa, AL 35487-0280, USA

ARTICLE INFO

Article history:
Received 16 August 2017
Received in revised form 7 May 2018
Accepted 30 May 2018
Available online 1 June 2018

Keywords:
Piezoelectric material
Multifunctional wing
Active control
Energy harvesting
Energy storage

ABSTRACT

In this paper, a highly flexible multifunctional wing with embedded piezoelectric materials and thin-film battery cells for adaptive vibration control and energy harvesting is studied. It provides a description of the electro-aeroelastic equations of multifunctional wings with piezoelectric devices functioning as both actuators for active vibration control and energy harvesters. The energy harvesters also act as dampers for passive vibration control. An LQR controller is implemented for the feedback control of the piezoelectric actuators. The optimal selection of the pre-placed piezoelectric device configuration for efficient flutter suppression is explored by minimizing the state and control costs while maximizing the harvesting output. The priority of the multifunctional wing design is put on a capability of vibration alleviation than energy harvesting. In addition, an active control algorithm for gust alleviation adaptively switching piezoelectric device functions is developed. A multifunctional wing that takes advantage of both active actuation and energy harvesting is then numerically studied by exploring the state, control, and harvesting costs in different numerical simulations under gust disturbances and aeroelastic instabilities. Finally, an energy storage design using thin-film lithium-ion batteries is considered to accumulate the harvested energy from piezoelectric devices. The performance of the multifunctional wing with such energy storage device is also explored.

© 2018 Elsevier Masson SAS. All rights reserved.

1. Introduction

For several years, different high-altitude long-endurance (HALE) unmanned aerial vehicles (UAVs) have been developed for both military and civilian operations. HALE UAVs usually feature high aspect-ratio wings with a low structural weight fraction to facilitate their long-endurance flight. Because of the slenderness, such wings may undergo large deformations under normal operation conditions, resulting in geometrically nonlinear behaviors [1–4]. Hence, geometrical nonlinearity must be considered in the aeroelastic modeling of these vehicles [1,2,5–7].

Although many improvements on the flight performance have been accomplished, there is still a need for further development to push the flight envelope of HALE UAVs. Meanwhile, different techniques have been developed and applied to improve aircraft performance and to facilitate the long-endurance flight. For instance, multifunctional structural technologies [8] may bring revolutionary changes to aircraft structures. These structures are capable of performing multiple primary functions and can potentially improve the aircraft performance through consolidation of subsystem materials and functions [8,9]. Applications of active materials will enable multiple primary functions of an integral wing structure. As being considered in this paper, piezoelectric materials are one of the active materials that are widely used in new generation aircraft structures [10–14]. They feature the energy conversion capability between mechanical deformation and electric charge, as well as high-bandwidth and fast response. On one hand, anisotropic piezocomposite actuators [15,16] allow active actuation of wing structures, which may contribute to the control of the wing aeroelastic instability or provide alternative maneuvering loads in a wing morphing concept. On the other hand, piezoelectric transducers may also be used to build onboard energy harvesting devices [17]. In fact, one may take advantage of piezoelectric transduction to fulfill the dual functions of both wing actuation and energy harvesting. If such a multifunctional wing is designed to be adaptive to various flight conditions, the multiple functions of the wing may help to improve the aircraft flight performance by actively controlling the wing vibration and providing additional energy. Moreover, if the shunt damping effect associated with the energy harvesting is combined with the active control, the combined contributions may help to achieve more improvement in aeroelastic performance of the wing. In addition, an integral energy storage device can be considered to accumulate the harvested energy and recycle them for

* Corresponding author.
E-mail address: suw@eng.ua.edu (W. Su).

https://doi.org/10.1016/j.ast.2018.05.056
1270-9638/© 2018 Elsevier Masson SAS. All rights reserved.

Nomenclature

$\mathbf{A}$	Coefficient matrix for state vector in state-space system model
$\mathbf{B}$	Coefficient matrix for control input in state-space system model
B	Body reference frame
$\mathbf{B_{vh}}$, $\mathbf{B_{va}}$	Piezoelectric coupling matrix for harvester and actuator
$\mathbf{B^F}$, $\mathbf{B^M}$	Influence matrices for the distributed forces and moments
C_p	Capacitance of the energy harvesting system ..... F
$\mathbf{F^{dist}}$, $\mathbf{F^{pt}}$	Distributed and point forces
$\mathbf{g}$	Gravity acceleration column vector ..... m/s^2
$\mathbf{H}$	Coefficient matrix for disturbance (process noise) in state-space output model
h	Flight altitude ..... m
id	Element identifier of wing
J, J_S, J_C, J_E	Total system, state, control, harvested energy cost functions
$\mathbf{J_{h\varepsilon}}$, $\mathbf{J_{p\varepsilon}}$, $\mathbf{J_{\theta\varepsilon}}$	Jacobian matrix
$\mathbf{K}$	Control filter gain
$\mathbf{M_{FF}}$, $\mathbf{C_{FF}}$, $\mathbf{K_{FF}}$	Generalized inertia, damping, and stiffness matrices
$\mathbf{M_s}$, $\mathbf{C_s}$, $\mathbf{K_s}$	Discrete inertia, damping, and stiffness matrices of whole system
$\mathbf{M^{dist}}$, $\mathbf{M^{pt}}$	Distributed and point moments
$\mathbf{N}$	Influence matrix for the gravity force
$\mathbf{Q}$, $\mathbf{R}$	Penalty matrix for control input and state vector
Q_e	Total charge accumulated over the electrodes C
r	Weighting term for cost penalty matrix
R_e	Resistance of energy harvesting circuit ..... Ω
$\mathbf{R}_\mathrm{F}$	Components of the generalized load vector
s	Beam curvilinear coordinate ..... m
U_F	Flutter speed ..... m/s
U_∞	Freestream velocity ..... m/s
$\mathbf{u}$	Control input to system plant
$\mathbf{v_a}$	Actuation voltage of multifunctional system V
$\mathbf{v_h}$	Harvested voltage of multifunctional system V
w	Local beam frame resolved in B frame
$\mathbf{x}$	State vector of system plant
$\hat{\mathbf{x}}$	State vector estimate of system plant
x_a	Design variable of optimization
α	Angle of attack ..... degree
$\boldsymbol{\varepsilon}$	Total beam strain vector
$\boldsymbol{\varepsilon}_0$	Initial beam strain vector
ε_x	Extensional strain in beam members
κ_x, κ_y, κ_z	Twist, flat bending, and edge bending curvature of beam members 1/m
κ_{thres}	User-defined bending curvature threshold
κ_y^{steady}	Flat bending curvature of beam members at steady-state 1/m
$\boldsymbol{\lambda}$	Inflow states ..... m/s
σ_w	Dryden gust strength ..... m/s

Subscript

$h\varepsilon$	$\boldsymbol{h}$ vector with respect to the strain
$p\varepsilon$	Nodal position $\boldsymbol{p_w}$ with respect to the strain $\boldsymbol{\varepsilon}$
$\Theta\varepsilon$	Nodal rotation $\boldsymbol{\theta}$ with respect to the strain $\boldsymbol{\varepsilon}$

active control purpose. Sodano et al. [18,19] proposed such an integrated design with a rechargeable battery. Later on, energy storage structural composites embedding thin-film lithium energy cells in carbon/epoxy laminates were constructed by Pereira et al. [20,21].

It would seem that these multiple functions may interfere or conflict each other during the operation, in that the active control will reduce the wing vibration, which naturally reduces the possible energy output from the harvesters. However, if some vibration is allowed, provided that it does not harm the wing/aircraft performance, it can serve as a source of the energy harvesting. Therefore, it is essential to evaluate the tradeoff between the functions and find an optimal balance between them. More importantly, the best tradeoff may change with the instantaneous flight conditions and environment. Therefore, the design should be adaptive to the corresponding condition and allow for a shift of the weight of the functions in the tradeoff. Such a tradeoff design of a multifunctional wing can be obtained by performing a design optimization of the aeroelastic and control system under different flight conditions. From the above discussion, the objectives of the optimization may involve the minimization or maximization of some performance metrics. Therefore, the system design is considered as a multi-objective optimization problem. Various algorithms have been developed to solve multi-objective optimization problems [22–25]. For example, the nondominated sorting genetic algorithm II (NSGA-II) [25] can find multiple Pareto-optimal solutions in a single simulation with a computationally efficient approach using elitism.

In this paper, numerical studies on a piezoelectric multifunctional wing will be presented. The objective of this paper is to demonstrate the feasibility of multifunctional wings for improving the aeroelastic and flight performance of HALE UAVs. The multifunctional wing will be designed to control its vibrations, enhance its aeroelastic performance, and produce supplemental energy out of the controlled vibrations by proficiently utilizing the properties of the embedded piezoelectric materials. The previous studies [26–28] showed that this type of multifunctional wing might suppress the aeroelastic instability and alleviate gust perturbations while generating a certain amount of electric power. Therefore, in this paper, a comprehensive study involving control with an adaptive function switch for aeroelastic instability and gust perturbations will be performed (the control with an adaptive function switch is called “adaptive control” in the following discussions, which should not be confused with control algorithms with an adaptive controller). A multifunctional wing will be designed for flutter suppression with supplemental piezoelectric energy harvesting as a passive damper through a multi-objective optimization. In addition, an adaptive algorithm to effectively alleviate vibrations due to stochastic gusts with various strengths will be developed by using a Linear Quadratic Regulator (LQR) [27,29]. Finally, an energy storage device is built into the wing, and its impact on the performance of the multifunctional wing will be explored. From the research, an adaptive multifunctional wing with optimized performed is highlighted. The hybrid system is also demonstrated to be partially energy self-sustainable. All these characteristics may significantly enhance the flight performance of the HALE aircraft.

2. Piezoelectric multifunctional wing model

A multifunctional wing model with embedded piezoelectric materials (e.g., Active Fiber Composites, AFC) is developed for the current studies based on what was studied in Refs. [27,28]. The multifunctional wing will be used to study both wing vibration control for improved aeroelastic performance and energy harvesting and storage that may supply additional operation power out

Table 1
Wing properties.

Airfoil	NACA0014
Span (cm)	400
Chord length (cm)	20
Reference axis location (from leading edge)	30% of chord
Center of gravity (from leading edge)	30% of chord

Table 2
Material properties for the wing model's cross-section (NACA0014).

	E-Glass	AFC
E_1 (GPa)	19.3	42.2
E_2 (GPa)	19.3	17.5
E_3 (GPa)	9.8	17.5
G_{12} (GPa)	4.1	5.5
G_{13} (GPa)	4.1	5.5
G_{23} (GPa)	3.28	4.4
ν_{12}	0.148	0.354
ν_{13}	0.148	0.354
ν_{23}	0.207	0.496
Thickness (mm)	0.1143	0.127
d_{11} (pm/V)	–	309
d_{12} (pm/V)	–	−129
Electrode distance (mm)	–	1.143

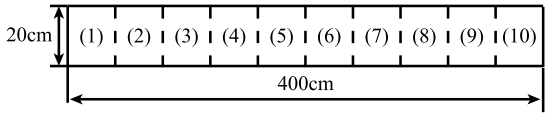

Fig. 1. Wing model dimensions and element IDs.

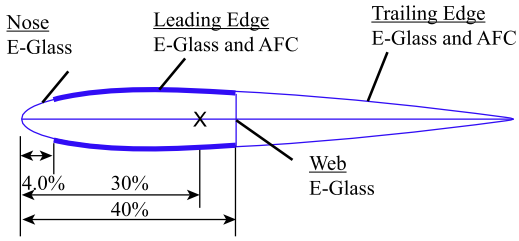

Fig. 2. Lay-up of the model wing's cross-section.

Table 3
Properties of the thin-film batteries (single battery pack).

Property	Value
Mass (g)	0.45
Energy density (Wh/L)	152.73
Thickness (mm)	0.1

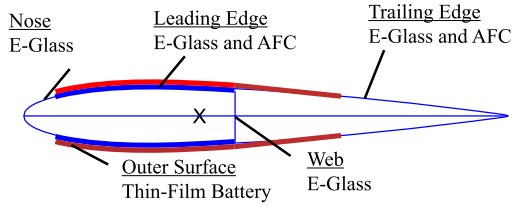

Fig. 3. Layups of the active wing cross-section with thin-film batteries.

of the controlled vibrations. By changing the electrical configuration of the wing, piezoelectric materials on a certain station along the wing can be utilized as either an actuator or a harvester. As discussed in the previous studies [26,27], the piezoelectric energy harvesting on the multifunctional wing can provide an additional function to serve as a damper (shunt damping effect), which enables passive vibration suppression/alleviation. Therefore, triple functions of the wing are first considered in the study, which are active bending/torsion actuation, passive shunt damping, and energy harvesting. As the primary objective of the wing design and study is the vibration suppression/alleviation to improve the wing performance, the function (as an actuator versus a harvester) of the piezoelectric materials at a spanwise location is mainly determined by the local magnitude of wing vibration. At the same time, piezoelectric materials configured as energy harvesting devices give power outputs from the controlled vibration. If the wing vibration magnitude is small and not harmful to the flight performance, the energy harvesting is fully activated on all the wing elements.

While the full wing properties described in Refs. [27,28], Tables 1 and 2 show the basic material and geometric properties of the wing. Fig. 1 shows the wing geometry and Fig. 2 is the layups of the wing cross-section. The wing is divided into ten elements, and the element identifiers (IDs) are assigned from the wing root to the tip ranging 1 to 10. The wing has a single wing spar located at 40% chord from the leading edge. The actuator orientations are at $\pm 22^\circ$ to have the balanced bending and torsional actuation capability [27,28]. The maximum actuation voltage of the wing is ± 2000 V, but this voltage limitation will be disabled in some of the following studies for performance comparison purpose. The resistive load R_e in the energy harvesting circuit of the wing is set as 1 MΩ.

An energy storage device is also considered to accumulate the power outputs from the harvester and to store them for discharge during vibration control. Thin-film lithium-ion batteries are applied for the energy storage, which are compatible with the piezoelectric devices [30]. By using the thin-film lithium-ion batteries, energy storage structural composites embedding thin-film lithium energy cells in carbon/epoxy laminates can be constructed. Such embedded thin-film energy cells do not significantly change the mechanical properties of the carbon/epoxy laminate including the stiffness and strength, although fracture properties of the material must be considered in design process [20,21]. The structural concept is to construct multi-layered composites by laminating thin-film battery layers for storing energy in addition to the active piezoelectric material layers. In the current study, properties of thin-film lithium-ion batteries produced by Front Edge Technologies are used for the following studies, with a mass of 0.45 g (single pack), a volume of 0.11 cm^3, and an energy density of 152.73 Wh/L [30] (see Table 3). Typically, the thickness of the thin-film batteries is 0.1 mm. By using the 70% chord length and the full span length as an initial design, the volume of the thin-film battery cells becomes 5.6×10^{-5} m^3 on the wing surface. If a bimorph structure is considered, the volume is doubled to 11.2×10^{-5} m^3 (0.112 L). Therefore, the total energy capacity is 17.11 Wh (61580.74 J). The additional weight due to the battery layers is 458.19 g. This design will be modified in the following study. Fig. 3 describes the multi-layered wing cross-section with active piezoelectric materials and thin-film batteries. Additional electrical circuit components (e.g., rectifier, regulator, controller, amplifier, etc.) for the piezoelectric energy harvesting/storage and the high-voltage piezoelectric actuation are also not considered. It is also assumed that energy dissipated in the battery charge and discharge (per cycle) between the piezoelectric composites and the thin-film batteries is 20% [31]. This 20% of energy loss is applied on discharging as the overall energy loss including the charging loss in the following study.

3. Theoretical formulation

In this section, a brief description of the electro-aeroelastic equations for highly flexible multifunctional wings [26–28] is pro-

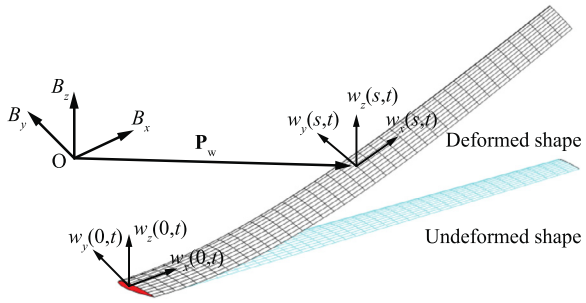

Fig. 4. Beam references frames.

vided. The piezoelectric actuation and energy harvesting are considered in a geometrically nonlinear wing model. An LQR [27,29] is designed for the feedback control of the wing. Optimum piezoelectric device configuration and active control of wing vibrations with an adaptive function switch can then be studied based on the formulation.

3.1. Electromechanical equations of motion

The coupled electro-aeroelastic finite-element equations for highly flexible wings (see Fig. 4) with embedded piezoelectric actuators and energy harvesters were introduced in [26–28], which are given as

$$\begin{aligned}&\mathbf{M_{FF}}\ddot{\boldsymbol{\varepsilon}} + \mathbf{C_{FF}}\dot{\boldsymbol{\varepsilon}} + \mathbf{K_{FF}}\boldsymbol{\varepsilon} = \mathbf{R_F}\\ &\mathbf{B_{vh}^T}\boldsymbol{\varepsilon} + C_p\mathbf{v_h} + Q_e = 0 \quad \text{or} \quad \mathbf{B_{vh}^T}\dot{\boldsymbol{\varepsilon}} + C_p\dot{\mathbf{v}}_\mathbf{h} + \mathbf{v_h}/R_e = 0\end{aligned} \tag{1}$$

The structural model features local strain degrees $\boldsymbol{\varepsilon}$ of each element to represent the large wing deformations, which includes extension ε_x, twist κ_x, and flat and edge bending curvatures κ_y and κ_z of the beam reference line. More details of the strain-based beam formulation can be found in Su and Cesnik [32]. In equation (1), the generalized inertia, damping, stiffness matrices and generalized force vector are

$$\begin{aligned}&\mathbf{M_{FF}}(\boldsymbol{\varepsilon}) = \mathbf{J_{h\varepsilon}^T M_s J_{h\varepsilon}} \qquad \mathbf{C_{FF}}(\boldsymbol{\varepsilon}, \dot{\boldsymbol{\varepsilon}}) = \mathbf{C}_s + \mathbf{J_{h\varepsilon}^T M_s \dot{J}_{h\varepsilon}}\\ &\mathbf{K_{FF}} = \mathbf{K_s}\\ &\mathbf{R_F} = \mathbf{K_{FF}}\boldsymbol{\varepsilon_0} + \mathbf{J_{h\varepsilon}^T N g} + \mathbf{J_{p\varepsilon}^T B^F F^{dist}}\\ &\qquad + \mathbf{J_{\theta\varepsilon}^T B^M M^{dist}} + \mathbf{J_{p\varepsilon}^T F^{pt}} + \mathbf{J_{\theta\varepsilon}^T M^{pt}} + \mathbf{B_{va}v_a} + \mathbf{B_{vh}v_h}\end{aligned} \tag{2}$$

in which $\boldsymbol{\varepsilon_0}$ is the initial strain of the beam. $\mathbf{B_{va}}$ and $\mathbf{B_{vh}}$ are the electromechanical coupling matrix for the piezoelectric actuator and harvester [26–28], respectively, and $\mathbf{v_a}$ and $\mathbf{v_h}$ are the corresponding actuation or harvested voltage, respectively. For simplicity, only the piezoelectric induced energy by wing vibrations in the flap bending direction is considered. Variables $\mathbf{g}$, $\mathbf{F^{dist}}$, $\mathbf{M^{dist}}$, $\mathbf{F^{pt}}$, and $\mathbf{M^{pt}}$ are the gravity field, distributed forces, distributed moments, point forces, point moments, respectively. $\mathbf{N}$, $\mathbf{B^F}$, and $\mathbf{B^M}$ are the influence matrices for the gravitational force, distributed forces, and distributed moments, which come from the numerical integration. In addition, Q_e is the total charge accumulated over the electrodes, whose time derivative is the current, C_p is the capacitance of the energy harvester, and R_e is the resistance of circuitry. The aerodynamic forces and moments ($\mathbf{F^{aero}}$ and $\mathbf{M^{aero}}$) are considered as a part of the distributed loads, which are calculated based on the Peters' finite-state inflow theory [33]. Jacobians $\mathbf{J}$ relating positions and rotations to the independent variable $\boldsymbol{\varepsilon}$ are obtained from the kinematics [5,32].

A cantilever beam is defined in a fixed frame B. To determine the position and orientation of each node along the beam reference line, a local beam frame w is built in the B frame (see Fig. 4). Bases of the beam frame w are $\mathbf{w_x}(s,t)$, $\mathbf{w_y}(s,t)$, and $\mathbf{w_z}(s,t)$, pointing along the beam reference axis, toward the leading edge, and normal to the beam surface, respectively. Those vectors are resolved in the B frame. The curvilinear beam coordinate s provides the nodal location in the body frame.

3.2. Active feedback control

Both LQR and LQG controllers have been designed in the previous active control studies of the multifunctional wing [27,28]. The detailed description can be found in Refs. [27,28]. For the design of the controllers, the nonlinear equations of motion in equation (1) need to be linearized about a nonlinear equilibrium [28]. Then the state-space model is derived as

$$\dot{\mathbf{x}} = \mathbf{Ax} + \mathbf{Bu} \tag{3}$$

where $\mathbf{x}$ is the state vector, $\mathbf{u}$ is the control input to the system plant. They are defined as

$$\mathbf{x} = \left\{ \boldsymbol{\varepsilon}^\mathbf{T} \quad \dot{\boldsymbol{\varepsilon}}^\mathbf{T} \quad \boldsymbol{\lambda}^\mathbf{T} \quad \mathbf{v_h^T} \right\}^\mathbf{T} \qquad \mathbf{u} = \mathbf{v_a} \tag{4}$$

where $\boldsymbol{\lambda}$ is the aerodynamic states from the two dimensional (2-D) finite-state inflow theory, developed by Peters and Johnson [33]. The voltages on each element $\mathbf{v_a}$ are controlled individually. The performance of the linear quadratic controllers depends on a combination of penalties in cost functions:

$$J = \int_0^\infty \left(\mathbf{x^T Q x} + r\mathbf{u^T R u}\right) dt \tag{5}$$

Ref. [27] implemented a simple controller design approach, where the weighting parameter r was determined by a tradeoff between the state cost and control cost. The control gain $\mathbf{K}$ for the LQR controller is determined by minimizing the cost function J and the control input $\mathbf{u}$ is obtained from

$$\mathbf{u} = -\mathbf{Kx} \tag{6}$$

In the design of LQG regulator, the feedback control is implemented with limited information about state variables obtained by a specific sensor (e.g., strain gauges or piezoelectric sensors). By taking into account the process and measurement noises of the system [27], the Kalman filter provides an estimated $\hat{\mathbf{x}}$ to the state $\mathbf{x}$, such that the control input is obtained as

$$\mathbf{u} = -\mathbf{K}\hat{\mathbf{x}} \tag{7}$$

Since the LQR controller performance can be recovered by adjusting the Kalman gain even the system uses the LQG controller with a limited number of state information, the LQR controller is used for gust alleviation and flutter suppression in the current study.

3.3. Adaptive function switch of multifunctional wing

The control gain can be appropriately defined for a predictable oscillation in a flight such as a flutter. However, such a fixed control gain may be less effective to uncertain disturbances like stochastic wind gusts. Therefore, an active control algorithm is considered in the current study, which is adaptive to the stochastic gusts. The algorithm allows the change of the number and position of actuators by monitoring the instantaneous bending curvatures, to achieve an efficient vibration alleviation under stochastic gust disturbances. Any elements that are not used as actuators are automatically switched to energy harvesting devices. The flatwise

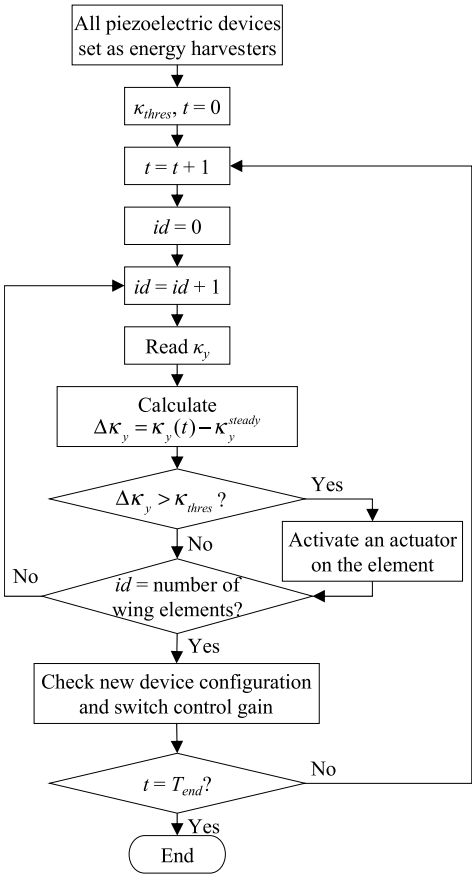

Fig. 5. Algorithm of the adaptive function switch.

bending and torsional vibrations of highly flexible wings are usually dominant. Therefore, it is effective to control these degrees to suppress/alleviate wing vibrations. The decision of whether or not to actuate one element for vibration control is made by the element's current flatwise bending curvature:

$$\Delta\kappa_y(t, id) = \kappa_y(t, id) - \kappa_y^{steady}(id) \tag{8}$$

where id is the element ID of the wing and κ_y^{steady} is the flatwise bending curvature at the steady-state. A flatwise bending curvature threshold is defined so that each element will be activated as an actuator when the difference between the flatwise bending curvature on an element at a particular time and its steady-state value exceeds the threshold. Feedback control gains for each activation configuration is calculated before the simulation, and the control gains can be switched when the actuation condition changes based on the instantaneous wing bending curvature. Fig. 5 shows the algorithm of the actuator activation and the control gain update for the active control.

3.4. Optimization of piezoelectric device configuration for the multifunctional wing

Even though the active controller with the adaptive function switch discussed in the previous section is designed for an effective vibration suppression under stochastic gusts, it is also desired that the controller can effectively suppress the flutter instability. If a controller designed by following the approach as mentioned earlier is directly applied for the flutter suppression, the nature of the design algorithm inevitably allows some initial development of vibration. In fact, for flutter suppression purpose, it is more effective to control the vibration immediately from its initial development of the instability. Therefore, the multifunctional wing should be such designed that a certain level of flutter suppression performance can be secured all the time when the flight speed is close or higher than the flutter speed. In doing so, some of the wing elements need to be fixed as regular actuators for flutter suppression when necessary. In this way, the active control is more robust for both flutter suppression and stochastic gust alleviation.

If one wants to achieve the most effective performance for flutter suppression, it is important to find an optimal selection of the pre-placed piezoelectric device configuration. Therefore, an optimization of the piezoelectric device configuration is performed. The optimization objective is to simultaneously obtain the maximum vibration suppression, the minimum control power input, and the maximum harvesting energy output out of the multifunctional wing. Therefore, the three objective functions of the optimization are defined as state cost J_S, control cost J_C, and harvested energy J_E, which are given as

$$\min J_S(x_a) = \int_0^\infty (\mathbf{x}^\mathbf{T}\mathbf{Q}\mathbf{x})dt \tag{9}$$

$$\min J_C(x_a) = \int_0^\infty (\mathbf{u}^\mathbf{T}\mathbf{R}\mathbf{u})dt \tag{10}$$

$$\max J_E(x_a) = \int_0^\infty (\mathbf{v}_\mathbf{h}^\mathbf{T} C_p \mathbf{v}_\mathbf{h})dt \tag{11}$$

where x_a is the design variable. A design constraint in the study is given in discrete choices as

$$x_a = [1, 2, \ldots, 10] \tag{12}$$

where design variable x_a includes IDs of elements to be assigned as regular actuators. More details about the constraint are given in the following section. Since there are only ten discrete-value design variables, the optimization is kept very simple by evaluating all the choices and choosing the best one, while the priority of the multifunctional wing design is put on a capability of vibration alleviation than energy harvesting.

4. Numerical studies

In this section, aero-servo-elastic analysis for the highly flexible multifunctional wing with adaptive vibration control and energy harvesting is performed, using the derived electro-aeroelastic formulation. The energy harvesters are also used as shunt dampers in passive vibration control. An LQR controller is implemented for the feedback control of the piezoelectric actuators. The optimal piezoelectric device configuration and controller for cost-effective active control is studied by evaluating the state, control, and harvesting costs in different numerical simulations under gust disturbances and aeroelastic instabilities. Finally, an energy storage design to accumulate harvested energy from piezoelectric harvesters for active control is considered using thin-film lithium-ion batteries, and energy management performance of the multifunctional wing is explored.

4.1. Flutter suppression with the optimal multifunctional wing

To properly understand the aeroelastic characteristics of the multifunctional wing designed in the previous section, flutter analyses are performed following the approach used in [28]. The flutter speed of the cantilevered multifunctional wing at different root angles of attack and altitude $h = 20{,}000$ m is given in Fig. 6. Three

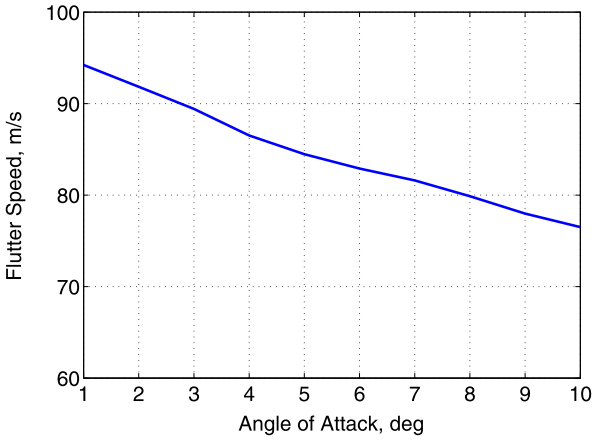

Fig. 6. Flutter characteristics with different angles of attack.

Dryden gust signals [26–28] with different strengths are generated to study the performance of the adaptive multifunctional wing under gust-involved flight conditions. The simulated gust and flight conditions are listed in Table 4. Fig. 7 describes the gust profile based on the power spectral density (PSD) with gust strength = 5 and 1.5 m/s at $U_\infty = 101.04$ m/s. The gust profile and PSD with gust strength = 1 m/s at $U_\infty = 45.93$ m/s are shown in Fig. 8. An aircraft may encounter such gusts with the strength of 5 m/s or 1 to 1.5 m/s 10^{-4} times or once per hour [34].

Table 4
Gust and flight conditions.

Gust model	1	2	3
Altitude h (m)	20,000	20,000	20,000
Flight speed U_∞ (m/s)	101.04	101.04	45.93
Gust strength σ_w (m/s)	1.5	5	1
Frequency band (Hz)	0.1–6	0.1–6	0.1–6
Length of gust signal (s)	30	30	600

First, it is verified that the LQR control performance for the multifunctional wing can be recovered using an LQG controller. The simulation is performed with a root angle of attack $\alpha = 5$ deg, altitude $h = 20{,}000$ m, and freestream velocity $U_\infty = 101.04$ m/s which is higher than the flutter speed. Gust model 1 is applied in the simulation, in which the wing encounters the gust from 0.1 to 4 s (i.e., the gust signal between 0.1 and 4 s in Fig. 7 is used). Consequently, the flight condition involves both gust perturbation and aeroelastic instability. For evaluation of the controllers' performance, all the wing elements are assigned as actuators. The desired LQR controller is configured with the weighting term $r = 1 \times 10^{-1}$ to have a balanced control performance of gust alleviation and actuation power. Furthermore, the LQG controller is set up by using the same LQR gain, while adjusting system matrix $\mathbf{H}$, and setting covariance matrices of the process and measurement noises for the Kalman filter, to recover the LQR performance.

The LQG control response becomes closer to the desired LQR control response with $\mathbf{H} = 0.1 \times \mathbf{I}$, where $\mathbf{I}$ is an identity matrix. Fig. 9 shows the vertical wing tip responses without any controllers and with the LQR and LQG controllers, respectively. Both

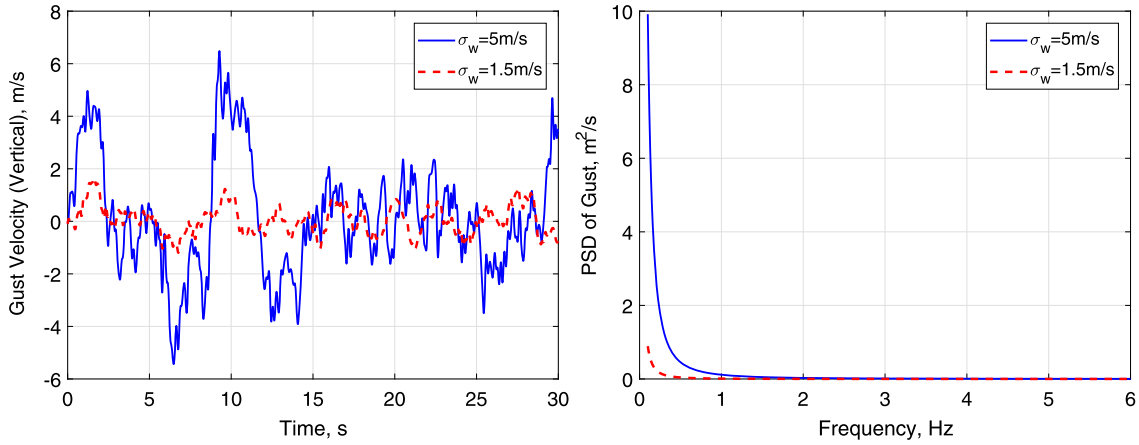

Fig. 7. Gust velocity and PSD function of gust turbulence with $\sigma_w = 5$ and 1.5 m/s at $h = 20{,}000$ m and $U_\infty = 101.04$ m/s.

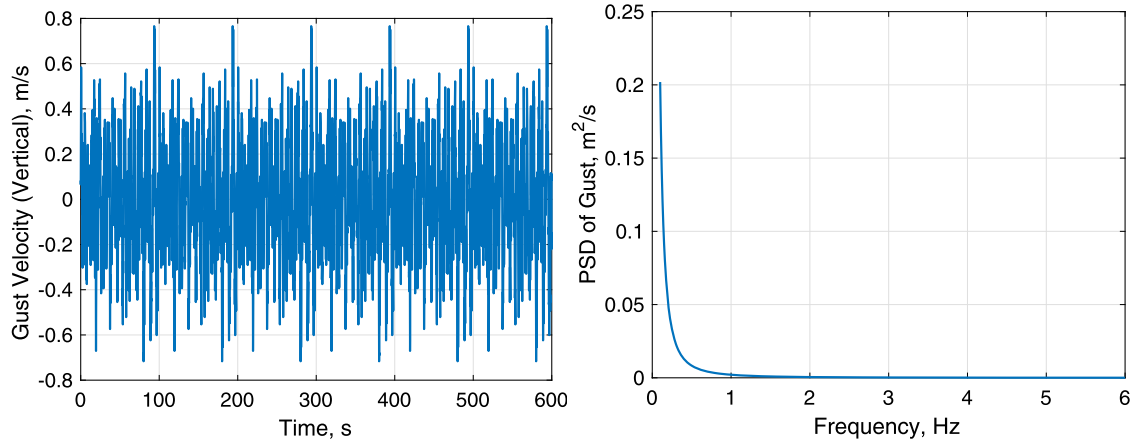

Fig. 8. Gust velocity and PSD function of gust turbulence with $\sigma_w = 1$ m/s at $h = 20{,}000$ m and $U_\infty = 45.93$ m/s.

Table 5
RMS voltage input (V_{rms}, V) on each element and total.

V_{rms} (V)	Element ID (from root)										Total
	1	2	3	4	5	6	7	8	9	10	
LQR	78.98	62.92	66.64	72.59	71.46	61.98	46.26	28.00	11.74	2.17	502.74
LQG	81.87	68.49	69.93	72.78	69.62	59.33	43.70	26.14	10.83	2.05	504.77

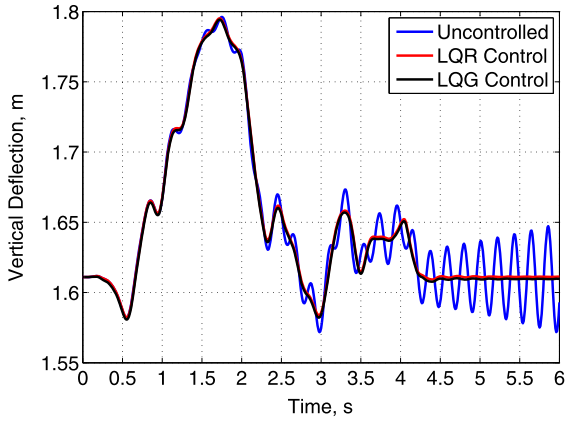

Fig. 9. Vertical wing tip responses of LQR and LQG controllers at $U_\infty = 101.04$ m/s ($h = 20{,}000$ m) with $\alpha = 5°$.

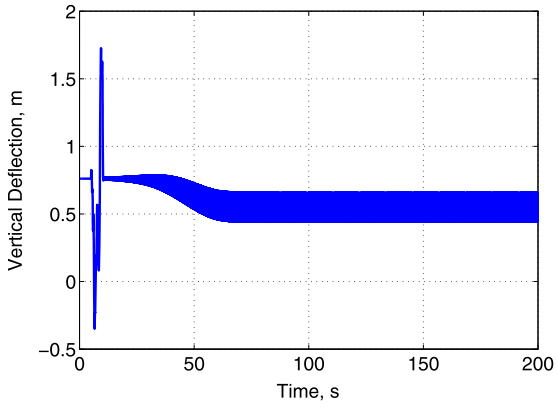

Fig. 10. Wing tip vertical deflection at $U_\infty = 101.04$ m/s ($h = 20{,}000$ m) with $\alpha = 2°$.

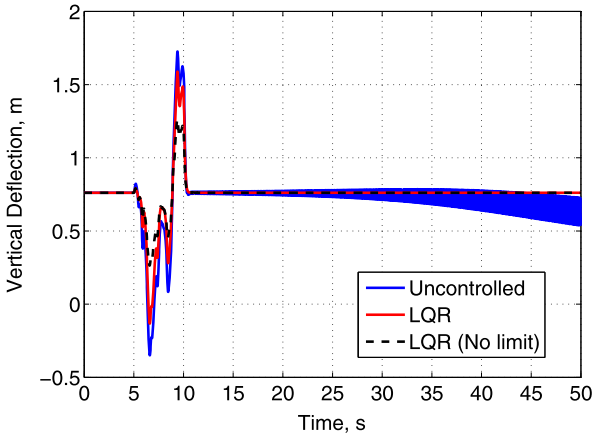

Fig. 11. Wing tip vertical deflection at $U_\infty = 101.04$ m/s ($h = 20{,}000$ m) with $\alpha = 2°$ with the LQR control.

controllers successfully suppress the flutter and alleviate high-frequency components of the wing vibration. Due to the setting with a relatively low control gain, the larger vibration with a low frequency is still observed. The state costs for both LQR and LQG controllers under the flow condition for 5 s are 760.31 J s and 759.19 J s, while the control costs are 19.184 kJ s and 19.632 kJ s. The differences of the state and control cost between the two controllers are 0.1% and 2.3%, respectively. Table 5 shows the root mean square (RMS) input voltage on each element for both controllers, while the simple summation of the RMS voltage outputs is called the total output [27,28]. Therefore, it can be seen that the two controllers have similar performances. It is also verified that an LQG controller can recover the desired LQR control performance of the multifunctional wing.

In the following studies, the root angle of attack is set at 2 deg, where the corresponding flutter speed U_F is 91.85 m/s. The freestream velocity $U_\infty = 101.04$ m/s, which is 10% higher than the flutter speed, is chosen for the study. To consider active control of the wing with both a gust perturbation and aeroelastic instability, Gust model 2 is applied in the simulation, in which the wing encounters the gust from 5 to 10 s. Fig. 10 shows the wing tip vertical deflection from the simulation with an LQR controller. With the consideration of the full performance of the actuator, all the wing elements are assigned as actuators. In this study, the weighting value for control penalty is set as $r = 2.069 \times 10^{-8}$ so that it gives a robust suppression of wing vibrations. Since the wing deflection at the freestream velocity is large, the actuation voltage reaches the maximum actuation voltage, 2000 V [27,28] under such a gust perturbation. Therefore, the effectiveness of the gust alleviation is limited, but the controller is still effective to suppress the flutter as shown in Fig. 11. For comparison purpose, the wing tip response without control input saturation is also shown in Fig. 11, in which a much larger reduction of the wing tip deflection can be observed.

There are two types of excitations in the above case, the external gust disturbance and the self-excitation due to the instability. Since the flutter is more predictable (in terms of the frequency and magnitude), a fixed actuator placement for the flutter suppression is considered first. The primary objective of the multifunctional wing design is the vibration suppression with the minimum required actuation energy. Therefore, one needs to use the minimum number of actuators on the wing. In this case with both gust and instability, it is shown that one actuator is sufficient to suppress the flutter based on a series of simulations with different actuation conditions as shown in Fig. 12. The numbers in the legends indicate element IDs actuated with the LQR controller (e.g., "LQR 1-2" means the first two elements from the wing root are activated). Although the configuration with a single actuator at the root (element ID = 1) can suppress the flutter well, the combined performance of the required control power, energy of wing vibrations under control, and amount of harvested energy may vary, which depends on the locations of actuators for the vibration control. Such locations of actuators, in turn, change the other wing subsystems (piezoelectric damping and energy harvesting). Therefore, a simple optimization is performed to find out the best location of the constant actuator among the ten elements. Table 6 shows the three costs related to the multifunctional wing with different placement of the regular actuator. The result with an actuator on the 9th element is omitted since the case becomes unstable. The cases with an actuator on the Elements 3–5, or 10 also grow gradually to be unstable after the gust encounters. With the con-

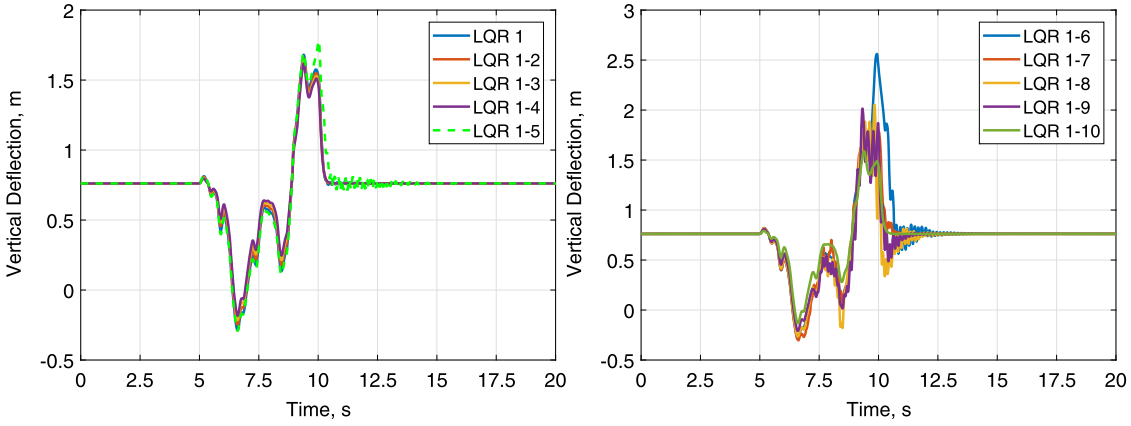

Fig. 12. Wing tip vertical deflection at $U_\infty = 101.04$ m/s ($h = 20{,}000$ m) with $\alpha = 2°$ with the LQR controls.

Table 6
System costs with different actuator placement.

Placed element	1	2	3	4	5	6	7	8	9	10
Output energy J_E (J s)	1.209	1.498	2.589	2.685	4.034	1.996	2.023	2.035	–	5.462
Control cost J_C (J s)	0.357	0.312	0.918	1.184	1.443	0.246	0.286	0.314	–	3.676
State cost J_s (J s)	1284.7	1284.5	1481.5	1458.1	1617.1	1287.4	1288.1	1288.7	–	2149.6

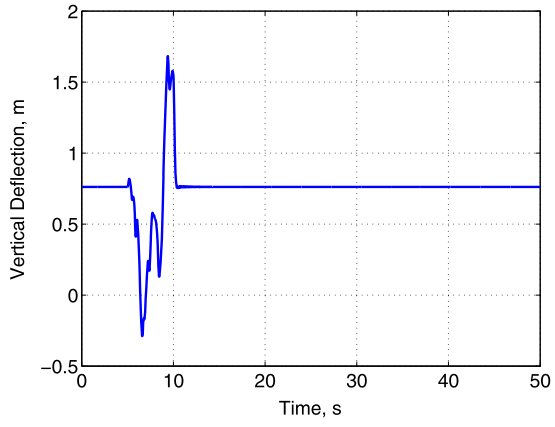

Fig. 13. Wing tip vertical deflection at $U_\infty = 101.04$ m/s ($h = 20{,}000$ m) with $\alpha = 2°$ with the LQR control on the second-root actuator.

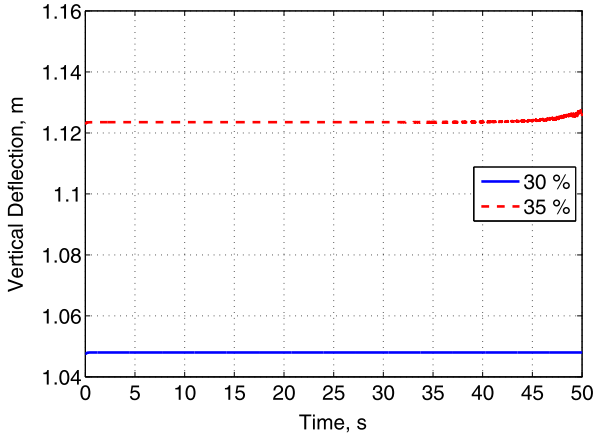

Fig. 14. Wing tip vertical deflection at $U_\infty = 119.41$ m/s and 124.00 m/s ($h = 20{,}000$ m) with $\alpha = 2°$ with the LQR control on the second-root actuator.

sideration of a balance of the stability, input cost, and output cost, the second element from the root of the wing is chosen to be the regular actuator in the following study. Again, the priority of the multifunctional wing design is put on a capability of vibration alleviation than energy harvesting. With only the second element being used as an actuator while other elements are used as harvesters, the wing response is shown in Fig. 13, which highlight that the flutter is successfully suppressed.

For further exploration on the new flutter boundary of the wing with the flutter suppression device, another series of time-domain simulations with different flight speeds are performed. Fig. 14 shows the wing tip deflections where the freestream speeds are 30% and 35% higher than the original flutter boundary, respectively. Again, the second element from the wing root is a regular actuator. As can be seen, if the freestream speed is no higher than 1.3 times the original flutter boundary, the single regular actuator can still successfully control the vibration. If the speed is further increased to 1.35 times the original flutter boundary, the growth of the vibration magnitude can be detected after 35 s. Therefore, the new flight boundary is increased to about 119.41 m/s from the original 91.85 m/s.

4.2. Adaptive actuator activation

In this section, the wing performance with active control and adaptive function switch to alleviate stochastic gusts is studied. Bending curvature thresholds are defined first as they are required by the algorithm to update the actuation status on each element. Fig. 15 shows the flatwise bending curvature variations from the steady-state on each element under the same flight condition as the previous section. The current curvature thresholds are defined as 20% of the maximum curvature variation on each element in Fig. 15 to activate the adaptive actuators under large wing deflections.

According to Fig. 15, the curvature is larger at locations closer to the wing root. Therefore, the inner-board elements are more effective in the vibration control. In this study, the inner-four elements are considered as adaptive active actuators. According to Ref. [27], an active control using only the inner-half elements was sufficient to alleviate the gust perturbation. However, for this wing model, the active control with the inner-half actuators does not perform as well as the control with only four elements, as shown in Fig. 16. In Fig. 16, “No control” represents wing tip vertical deflection without any controls. “LQR 1-4” means that inner four

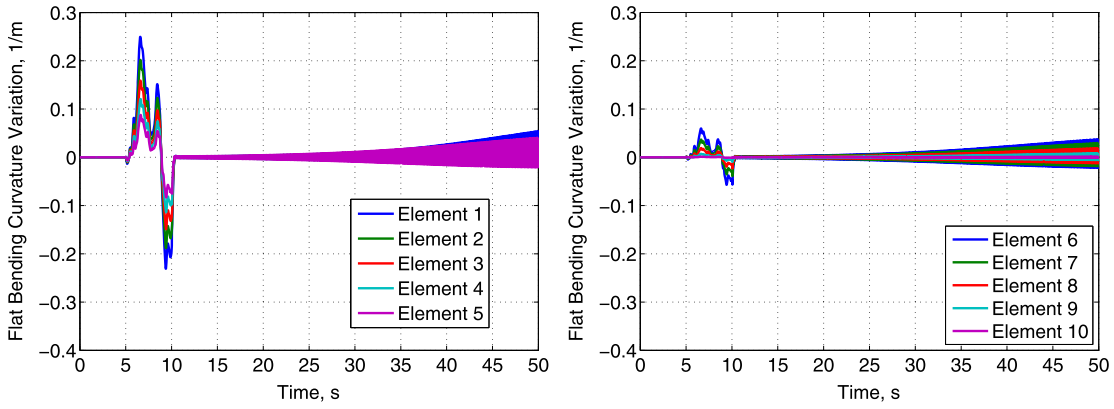

Fig. 15. Flat bending curvature variation histories on each element over time.

Table 7
Activating configurations.

Element ID	1	2	3	4
Activation case 1	On	On	Off	Off
Activation case 2	Off	On	Off	Off
Activation case 3	Off	On	On	Off
Activation case 4	Off	On	Off	On
Activation case 5	On	On	On	Off
Activation case 6	On	On	Off	On
Activation case 7	Off	On	On	On
Activation case 8	On	On	On	On

Table 8
Conditions of activation status.

Activation status	Condition
On	$\Delta\kappa_y(t, id) > \kappa_{thres}(id)$
Off	$\Delta\kappa_y(t, id) < \kappa_{thres}(id)$

elements are used as actuators. The remaining labels are similarly defined. In fact, the state cost reduction by the inner-four actuators with respect to the uncontrolled vibration over the initial 11 s is 34.35%. The amount of the state cost reduction is close to the state cost reduction by the full-span actuators, which is 38.32%. On the other hand, the control cost with the full-span actuators is 7.36×10^7 Js, while the control cost with the inner-four actuators is 5.98×10^7 Js which is 18.75% lower than the full-span actuation. Therefore, the setting with inner-four elements as actuators can provide a more cost-effective gust alleviation for this case.

In addition, the second element from the wing root is already assigned as the regular actuator for the flutter suppression. Therefore, the first, third, and fourth elements from the root are interchangeable between actuator and energy harvester during the flight. When an element is not actuated, it works as an energy harvester automatically. Since the three elements are used as the adaptive actuators and the second element is used as the regular actuator, there are eight combinations for the actuation configurations as listed in Table 7. Table 8 describes the conditions of the activation status on each element in which $\Delta\kappa_y$ is calculated from equation (8), and κ_{thres} is the user-defined bending curvature threshold to specify the deflection amount of the wing. Eight LQR gains for each configuration are calculated beforehand, and the control gains are switched when the activating configuration changes based on the curvature monitoring.

4.3. Performance of adaptive active control and energy harvesting

In this section, a study of the adaptive multifunctional wing with both the active control and energy harvesting is presented, where the effectiveness of flutter suppression, gust alleviation, and

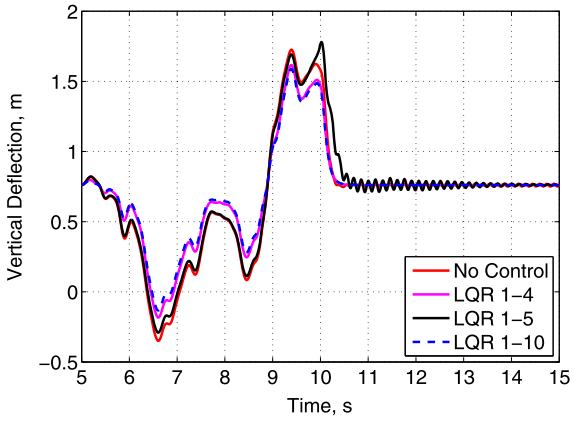

Fig. 16. Wing tip vertical deflection with different actuator configurations.

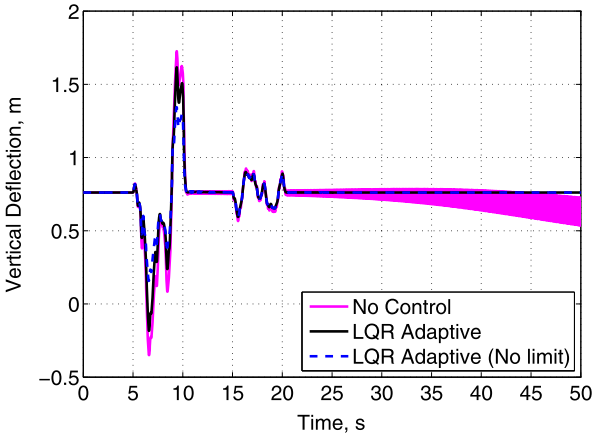

Fig. 17. Wing tip vertical deflection at $U_\infty = 101.04$ m/s ($h = 20{,}000$ m) with $\alpha = 2°$ under the two gusts flight case with/without the adaptive LQR control.

the voltage output from the multifunctional wing will be simultaneously explored.

For the performance evaluation, Gust 1 and Gust 2 described in the previous section are used here, in which the wing encounters Gust 2 between 5 and 10 s and then Gust 1 between 15 and 20 s. The freestream velocity U_∞ is 101.04 m/s. Fig. 17 shows the wing tip deflections with the control and the adaptive function switch. For comparison purpose, the adaptive control without the actuation voltage saturation is also plotted to see the control capability without the material constraint. It can be seen that the adaptive control alleviates the wing vibration under Gust 2 when the curvature thresholds are exceeded. The control effort is weak when the

Table 9
RMS power input/output (P_{rms}, mW) on each element and total.

P_{rms} (mW)	Element ID (from root)										Total
	1	2	3	4	5	6	7	8	9	10	
Actuator input	275.4	312.4	255.6	238.9	–	–	–	–	–	–	4318.5
Harvester output	0.480	–	0.328	0.249	0.631	0.287	0.108	0.029	0.004	0	13.477

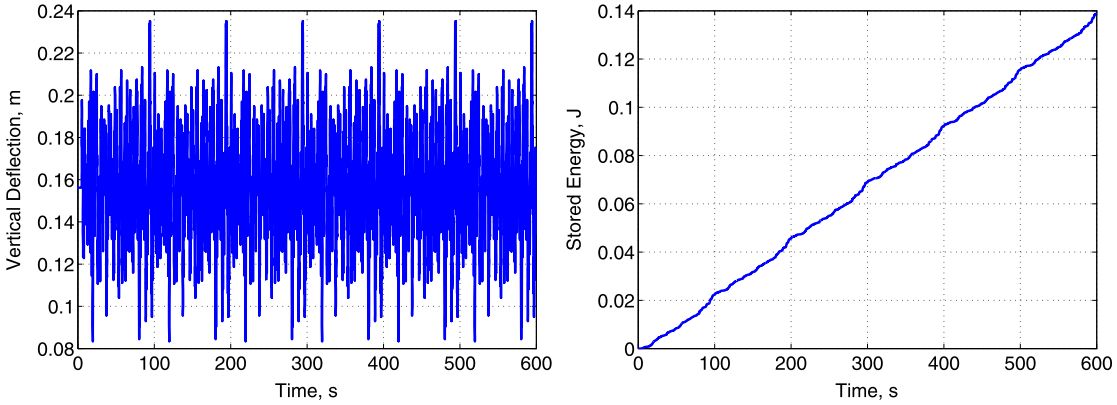

Fig. 18. Wing tip vertical deflection and energy storage time history at $U_\infty = 45.93$ m/s ($h = 20{,}000$ m) with $\alpha = 2°$ with the energy harvesting and without the LQR control under the empty storage condition.

curvature thresholds are not exceeded under Gust 1, in which only the second element from the root is used for the vibration control. Also, the flutter after the gust encounters is suppressed with only the second element actuated. The three system costs for the flight case over 50 s are 61.4766 J s for the state cost, 5.4127×10^7 J s for the control cost, and 0.3383 J s for the harvested energy, respectively.

Table 9 shows the RMS power input for each actuator and the power output from harvesters. In addition, the power output amount over 13 mW is sufficient to support other device operation, or it can be used for the actuators to save the energy consumption.

4.4. Multifunctional wing with active actuation, energy harvesting, and energy storage

The performance of the wing with the integral energy storage is evaluated at pre- and post-flutter speed, with different wind gusts. The freestream velocity U_∞ is 101.04 m/s (10% higher than the flutter boundary $U_F = 91.85$ m/s), or 45.93 m/s (50% lower than the flutter boundary). The root angle of attack is 2 deg. The maximum energy storage limit is 17.11 Wh, or 61580.74 J. When the stored energy in the battery cells becomes zero, no actuation can be performed. In addition, no more energy is accumulated in the energy storage if the stored energy reaches the maximum energy storage capacity, which means only the shunt damping is used for passive vibration control.

The charge on the battery cells by energy harvesting is first evaluated with a flight at 45.93 m/s under a persistent weak gust (Gust 3 in Table 4 with gust strength σ_w of 1 m/s) encountered from 5 s. The wing tip vertical deflection with no controllers but full-span harvesters is given in Fig. 18. The harvested energy is also shown in Fig. 18. With the wing vibration under the persistent gust for 600 s, the energy of 0.1388 J is accumulated.

Next, the energy consumption with the gust alleviation at $U_\infty = 45.93$ m/s is studied. Gust 3 is encountered between 3 and 4 s. The weight value of the LQR control is 2.08×10^{-8}. The curvature thresholds of the function switch for the piezoelectric device are set as 5% of the curvatures under the steady-state flight. The energy harvesting is activated, but the battery is initially charged fully up to 61580.74 J. Fig. 19 shows the wing tip vertical deflections with and without the adaptive LQR controller and the time history of the energy storage. The state costs without and with the adaptive LQR control are 0.013 J s and 0.0083 J s, respectively. Therefore, the state cost reduction by the adaptive LQR control with respect to the uncontrolled vibration is 37.84%, and the LQR controller has successfully alleviated the wing vibration due to the gust. According to the result, the wing discharged energy of 0.021 J for the short gust alleviation under the flight speed lower than the flutter boundary.

Finally, the stored energy change with the flutter suppression and gust alleviation at $U_\infty = 101.04$ m/s is investigated. Gusts 1 and 2 in Table 4 are encountered from 5 to 10 s and 15 to 20 s, respectively. The weight value of the LQR control is again 2.08×10^{-8}. The curvature thresholds for the adaptive piezoelectric actuation are set as 1% of the steady-state curvatures. The battery cells are still fully charged up to 61580.74 J before the simulation. The energy harvesting provides additional energy during the flight as the active control consumes the energy. Fig. 20 plots the wing tip vertical deflections with and without the adaptive LQR controller and the time history of the energy storage. The state cost is reduced by 74.46% when the adaptive LQR control is used. Therefore, the LQR controller successfully suppresses the post-flutter limit-cycle oscillation and alleviates the wing vibration due to the gust perturbation. The energy discharge between 5 and 15 s, which is under the strong gust with the flight speed higher than the flutter boundary, is 801.15 J. In addition, the energy of 7.49 J is used between 15 and 25 s under the weak gust for the vibration control. Also, the flutter suppression consumes 5.95×10^{-5} J between 25 and 50 s. This small energy consumption is the benefit from the regular actuator for the flutter suppression. Since the regular actuator starts to suppress vibration from the initial growth of the vibration due to the instability, the required energy is much lower than that for the flutter suppression after a fully developed limit-cycle oscillation (LCO). Fig. 21 shows the wing tip vertical deflection with a flutter suppression when the controller is turned on at 80 s after the LCO is fully developed. As can be seen, the adaptive control can still suppress the fully developed flutter. However, as shown in Fig. 21, much more significant energy is required to suppress the fully developed LCO

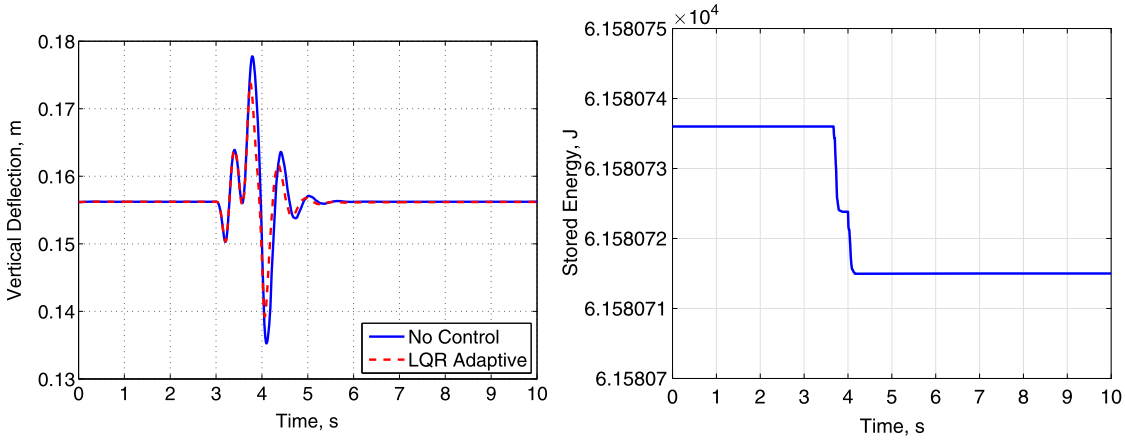

Fig. 19. Wing tip vertical deflection with and without the adaptive LQR control and energy storage time history at $U_\infty = 45.93$ m/s ($h = 20{,}000$ m) with $\alpha = 2°$ under the full storage condition.

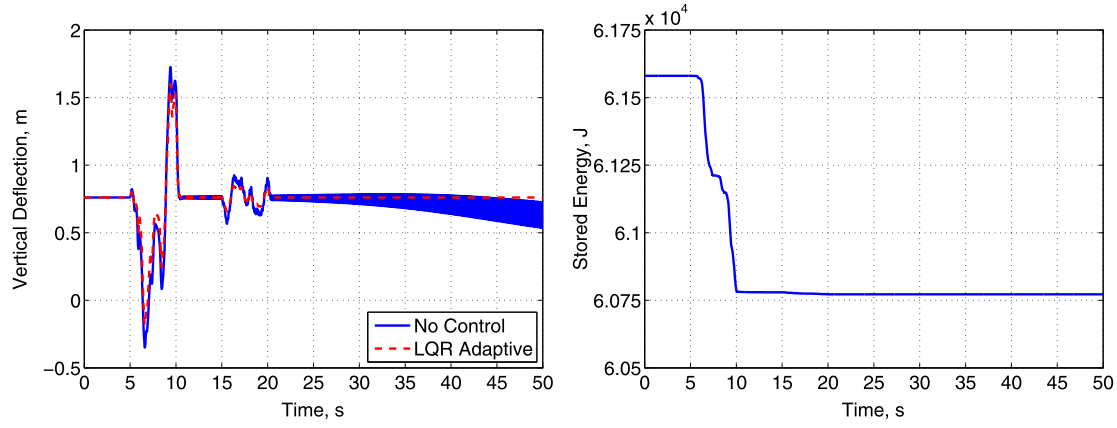

Fig. 20. Wing tip vertical deflection at $U_\infty = 101.04$ m/s ($h = 20{,}000$ m) with $\alpha = 2°$ with and without the LQR control and energy storage time history under the full storage condition.

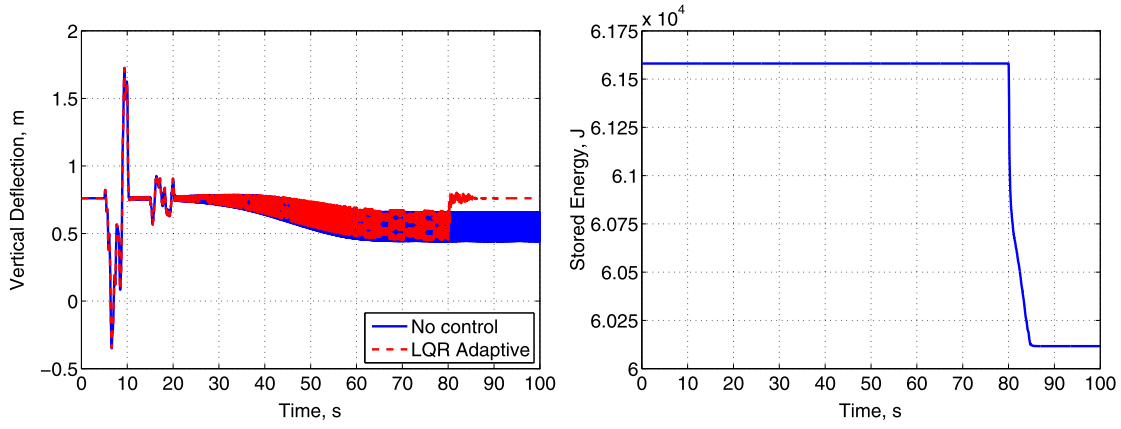

Fig. 21. Wing tip vertical deflection at $U_\infty = 101.04$ m/s ($h = 20{,}000$ m) with $\alpha = 2°$ with and without the LQR control (turned om at 80 s) and energy storage time history under the full storage condition.

than the energy for flutter suppression with the regular actuator (Fig. 20). Therefore, the implementation of the regular actuator is more cost-effective for flutter suppression.

A summary of the energy change with the piezoelectric energy harvesting and active control is given in Table 10. Herein, a 20% of energy loss on discharging is applied. By considering the energy harvesting performance under the persistent gust at the flight speed lower than the flutter boundary for 600 s, the average harvested energy is 2.31×10^{-4} J/s. On the other hand, the energy consumption for the gust alleviation under the flutter speed is 0.025 J. Thus, it will take 109.09 s to charge enough to support the gust alleviation. Also, the flutter suppression for 25 s at the flight speed, which is 10% higher than the flutter speed, requires the energy consumption of 7.14×10^{-5} J. This energy amount can be accumulated in less than one second by the energy harvesting under the flutter speed with the persistent gust. In addition, the discharges of the flutter suppression and the alleviations of two types of wind gusts are 961.38 J and 8.99 J, respectively. Charg-

Table 10
Stored energy change.

Simulation case	Energy change (J)	Time (s)	Average harvested energy (J/s)
Energy harvesting	+0.14	600	2.31×10^{-4}
Adaptive gust alleviation under flutter boundary	−0.025	10	–
Flutter suppression	-7.14×10^{-5}	25	–
Adaptive gust alleviation over flutter boundary (strong gust)	−961.38	10	–
Adaptive gust alleviation over flutter boundary (weak gust)	−8.99	10	–

ing time for both alleviations is more than 10.00 h. Therefore, an energy accumulation for a short-duration gust alleviation under flutter boundary or a flutter suppression without gust disturbances can be performed during a flight in less than two minutes with the energy harvesting. However, to activate adaptive active controls for the simultaneous flutter suppression and gust alleviation over flutter boundary, the battery cells should be charged enough to support high energy consumptions before a flight. In addition, to store the energy required to support the simultaneous flutter suppression and the gust alleviations, the bimorph thin-film battery should cover 1.14% of the wing upper and lower surfaces along the span. This design costs 7.74 g of an additional weight, which is 0.47% of the wing weight, to the original wing without battery layers. Thus, the weight cost of the extra batteries can be neglected. Based on the observations with the thin-film battery cells, the multifunctional wing can provide a partially self-sustained energy management capability.

5. Conclusion

A multifunctional wing with embedded anisotropic piezoelectric materials and thin-film lithium-ion battery cells for wing vibration suppression and energy harvesting was studied in this paper. The objective of this paper was to demonstrate the feasibility of piezoelectric multifunctional wings to enhance the aeroelastic and flight performance of HALE UAVs. The quadruple functions, including active bending/torsion actuation, piezoelectric damping, energy harvesting, and energy storing, were achieved for the wing. An approach for the integrated modeling of energy harvesting from wing transient vibrations and active bending/torsional actuation using anisotropic piezoelectric materials was introduced. The strain-based geometrically nonlinear beam formulation was coupled with an electromechanical model of the active and passive piezoelectric effects. The coupled electro-aeroelastic model enabled the prediction of the transient electric outputs and the mechanical deformations of the electro-aeroelastic system under aeroelastic instabilities and external excitations. The LQR controller was mainly implemented for the feedback control of the piezoelectric actuation to optimize the total wing performance. A control algorithm to adaptively change the actuation condition and update the control gain to achieve cost-effective feedback control performance was also developed. The piezoelectric device configuration on the multifunctional wing was optimized to keep a cost-effective performance of a constant flutter suppression. For practical applications of piezoelectric energy harvesting, the integrated multifunctional wing was designed to accumulate the harvested energy in the thin-film battery cells and recycle the stored energy for active flutter suppression and gust alleviation.

From energy harvesting with the thin-film battery cells, energy can be harvested and accumulated with the wing vibrations due to either wind gust excitations or flutter instability. However, the thin-film battery cells should be highly charged before the flight for adaptive and active controls on the simultaneous flutter suppression and gust alleviation above flutter boundary. This is because of the high energy consumptions in the latter cases. It is noted that the current work was completed based on several simplifications on the multifunctional wing. For example, the electric circuit for the regulation of the harvested energy was not involved. An 20% energy loss during the cycle of charging and discharging of battery packs was considered. Additionally, the layups of the piezoelectric materials embedded in the wing can be further optimized for better actuation and harvesting performances. However, the current work still provided insights into the studies of highly flexible multifunctional wings. First, it provided a synergy of the electro-aeroelastic formulation with the adaptive control algorithm, especially for highly flexible piezoelectric wings featured in HALE UAVs. The multifunctional wing, with both an optimized piezoelectric device configuration and an adaptive control algorithm, may not only successfully suppress the flutter and extend the flight envelope, but also alleviate vibrations due to external wind gusts. By adjusting the bending curvature threshold, one can specify the wing deflection amount under control. The allowed wing vibration would be able to provide an output voltage from energy harvesting subsystem, which may be used as additional energy for aircraft operations. With the proposed multifunctional wing design integrated with piezoelectric composites and thin-film battery cells, a partially self-sustained system can be realized similar to a hybrid system of the type used in automobiles. For example, the power output from energy harvesting can be accumulated in an energy storage device when the control is turned off, and the stored energy can be recycled for a short-duration actuation to suppress/alleviate wing vibrations due to flutter or wind gusts.

Conflict of interest statement

There is no conflict of interest.

References

[1] M.J. Patil, D.H. Hodges, C.E.S. Cesnik, Nonlinear aeroelasticity and flight dynamics of high-altitude long-endurance aircraft, J. Aircr. 38 (2001) 88–94.
[2] C.M. Shearer, C.E.S. Cesnik, Nonlinear flight dynamics of very flexible aircraft, J. Aircr. 44 (2007) 1528–1545.
[3] W. Su, C.E.S. Cesnik, Nonlinear aeroelasticity of a very flexible blended-wing-body aircraft, J. Aircr. 47 (2010) 1539–1553.
[4] W. Su, C.E.S. Cesnik, Dynamic response of highly flexible flying wings, AIAA J. 49 (2011) 324–339.
[5] C.E.S. Cesnik, E.L. Brown, Modeling of high aspect ratio active flexible wings for roll control, in: 43rd AIAA/ASME/ASCE/AHS Structures, Structural Dynamics, and Materials Conferences, AIAA Paper 2002-1719, Denver, CO, Apr. 22–25, 2002.
[6] C.E.S. Cesnik, W. Su, Nonlinear aeroelastic modeling and analysis of fully flexible aircraft, in: 46th AIAA/ASME/ASCE/AHS/ASC Structures, Structural Dynamics, and Materials Conference, AIAA, Austin, TX, Apr. 18–21, 2005.
[7] C.-S. Chang, D.H. Hodges, M.J. Patil, Flight dynamics of highly flexible aircraft, J. Aircr. 45 (2008) 538–545.
[8] L. Christodoulou, J.D. Venables, Multifunctional material systems: the first generation, JOM 55 (2003) 39–45.
[9] S.R. Anton, A. Erturk, D.J. Inman, Multifunctional unmanned aerial vehicle wing spar for low-power generation and storage, J. Aircr. 49 (2012) 292–301.
[10] P. Panda, Piezoceramic materials and devices for aerospace applications, in: Aerospace Materials and Material Technologies, Springer, Singapore, 2017, pp. 501–518.
[11] S.B. Cumming, M.S. Smith, A. Ali, T.T. Bui, J. Ellsworth, C.A. Garcia, Aerodynamic flight test results for the adaptive compliant trailing edge, in: AIAA Atmospheric Flight Mechanics Conference, AIAA Paper 2016-3855, Washington, DC, Jun. 13–17, 2016.

[12] M.S. Smith, T.T. Bui, C.A. Garcia, S.B. Cumming, Longitudinal aerodynamic modeling of the adaptive compliant trailing edge flaps on a GIII aircraft and comparisons to flight data, in: AIAA Atmospheric Flight Mechanics Conference, AIAA Paper 2016-3703, Washington, DC, Jun. 13–17, 2016.
[13] A. Raghavan, C.E. Cesnik, Review of guided-wave structural health monitoring, Shock Vib. Dig. 39 (2007) 91–116.
[14] S.S. Kessler, S.M. Spearing, Design of a piezoelectric-based structural health monitoring system for damage detection in composite materials, in: Smart Structures and Materials 2002: Smart Structures and Integrated Systems, SPIE, San Diego, CA, Mar. 2002, pp. 86–96.
[15] A.A. Bent, Active fiber composite material systems for structural control applications, in: Smart Structures and Materials 1999: Industrial and Commercial Applications of Smart Structures Technologies, SPIE, Newport Beach, CA, Mar. 2–4, 1999, pp. 166–177.
[16] R.B. Williams, G. Park, D.J. Inman, W.K. Wilkie, An overview of composite actuators with piezoceramic fibers, in: 20th International Modal Analysis Conference, Los Angeles, CA, 2002, pp. 421–427.
[17] A. Erturk, D.J. Inman, Piezoelectric Energy Harvesting, John Wiley & Sons, Hoboken, NJ, 2011, pp. 1–94, 151–385.
[18] H.A. Sodano, D.J. Inman, G. Park, Generation and storage of electricity from power harvesting devices, J. Intell. Mater. Syst. Struct. 16 (2005) 67–75.
[19] H.A. Sodano, D.J. Inman, G. Park, Comparison of piezoelectric energy harvesting devices for recharging batteries, J. Intell. Mater. Syst. Struct. 16 (2005) 799–807.
[20] T. Pereira, Z.H. Guo, S. Nieh, J. Arias, H.T. Hahn, Energy storage structural composites: a review, J. Compos. Mater. 43 (2009) 549–560.
[21] T. Pereira, Z.H. Guo, S. Nieh, J. Arias, H.T. Hahn, Embedding thin-film lithium energy cells in structural composites, Compos. Sci. Technol. 68 (2008) 1935–1941.
[22] K. Deb, Multi-Objective Optimization Using Evolutionary Algorithms, John Wiley & Sons, Chichester, U.K., 2001.
[23] C.M. Fonseca, P.J. Fleming, An overview of evolutionary algorithms in multiobjective optimization, Evol. Comput. 3 (1995) 1–16.
[24] J. Branke, K. Deb, K. Miettinen, R. Slowiński, Multiobjective Optimization: Interactive and Evolutionary Approaches, Springer, New York, NY, 2008.
[25] K. Deb, A. Pratap, S. Agarwal, T. Meyarivan, A fast and elitist multiobjective genetic algorithm: NSGA-II, IEEE Trans. Evol. Comput. 6 (2002) 182–197.
[26] N. Tsushima, W. Su, Modeling of highly flexible multifunctional wings for energy harvesting, J. Aircr. 53 (2016) 1033–1044.
[27] N. Tsushima, W. Su, Concurrent active piezoelectric control and energy harvesting of highly flexible multifunctional wings, J. Aircr. 54 (2016) 724–736.
[28] N. Tsushima, W. Su, Flutter suppression for highly flexible wings using passive and active piezoelectric effects, Aerosp. Sci. Technol. 65 (2017) 78–89.
[29] F.L. Lewis, V.L. Syrmos, Optimal Control, John Wiley & Sons, New York, NY, 1995.
[30] S.R. Anton, A. Erturk, D.J. Inman, Multifunctional self-charging structures using piezoceramics and thin-film batteries, Smart Mater. Struct. 19 (2010).
[31] N.J. Dudney, Thin film micro-batteries, Electrochem. Soc. Interface 17 (2008) 44.
[32] W. Su, C.E.S. Cesnik, Strain-based geometrically nonlinear beam formulation for modeling very flexible aircraft, Int. J. Solids Struct. 48 (2011) 2349–2360.
[33] D.A. Peters, M.J. Johnson, Finite-state airloads for deformable airfoils on fixed and rotating wings, in: Symposium on Aeroelasticity and Fluid Structure Interaction Problems, ASME Winter Annual Meeting, New York, NY, Nov. 6–11, The American Society of Mechanical Engineering, 1994, pp. 1–28.
[34] D. Moorhouse, R. Woodcock, US Military Specification MIL–F–8785C, US Department of Defense, Arlington County, VA, 1980.